The Green's function for the radiative transport equation in the slab geometry

The Green's function for the radiative transport equation in the slab geometry

Manabu Machida[1]**, George Y Panasyuk**[1]**, John C Schotland**[2] **and Vadim A Markel**[3]

[1] Department of Bioengineering, University of Pennsylvania, Philadelphia, PA 19104, USA
[2] Department of Bioengineering and Graduate Group in Applied Mathematics and Computational Science, University of Pennsylvania, Philadelphia, PA 19104, USA
[3] Department of Radiology, University of Pennsylvania, Philadelphia, PA 19104, USA

E-mail: schotland@seas.upenn.edu

Abstract

The radiative transport equation is solved in the three-dimensional slab geometry by means of the method of rotated reference frames. In this spectral method, the solution is expressed in terms of analytical functions such as spherical harmonics and Wigner d-functions. In addition, the eigenvalues and eigenvectors of a tridiagonal matrix and certain coefficients, which are determined from the boundary conditions, must also be computed. The Green's function for the radiative transport equation is computed and the results are compared with diffusion approximation and Monte Carlo simulations. We find that the diffusion approximation is not quite correct inside the slab, even when the light emitted from the slab is well described by the diffusion approximation. The solutions we obtain are especially convenient for solving inverse problems associated with radiative transport.

PACS numbers: 05.60.Cd, 87.57.Gg, 42.68.Ay, 95.30.Jx

1. Introduction

The radiative transport equation (RTE) is widely used to describe the propagation of multiply scattered light in random media including biological tissue, the atmosphere and the ocean [1–4]. Despite the fact that the RTE has been studied for decades, analytical solutions are known only for the case of isotropic scattering [5, 6]. In the latter case, in the presence of boundaries, solutions can only be obtained if the problem is effectively one dimensional. For example, an axially symmetric beam perpendicular to one or more planar interfaces can be described by a specific intensity which depends on one spatial and one angular variable. The case of one spatial and two angular variables was recently studied [7, 8] by using a method which relates multidimensional solutions of the RTE to solutions of the so-called pseudo-problem [9–11].

In many applications, especially those which arise in biomedical imaging, it is necessary to consider the RTE in three spatial dimensions with full angular variation. This five-dimensional problem is solved using numerical methods such as the discrete-ordinate method [12], the P_L approximation [5], the method of invariant embedding [3] or the Monte Carlo method [13]. The drawback of such methods is their extremely high computational cost.

In recent work [14, 15], we have described a spectral method for solving the three-dimensional RTE with anisotropic scattering. The method is applicable to geometries with planar boundaries and both internal and external sources. In this approach, the RTE Green's function is decomposed into plane-wave modes characterized by the wave vector **k**. Each mode is then expanded into spherical harmonics defined in a rotated reference frame whose z-axis is aligned with the direction $\hat{\mathbf{k}}$. We refer to this approach as to the method of rotated reference frames (MRRF). Kim and Keller [16, 17] have also studied the plane-wave decomposition of the RTE Green's function. However, in their work the angular dependence of Green's function is computed numerically as a basis of discrete ordinates.

Numerical studies of the MRRF have so far been limited to the case of an infinite medium [15]. In this paper, we use the MRRF to solve the three-dimensional RTE in a medium with planar boundaries (the slab geometry). This geometry is of considerable interest in applications to biomedical optical imaging, where plane-wave expansions are an important tool for the study of the inverse transport problem [18, 19].

The remainder of this paper is organized as follows. In section 2, we recall some aspects of radiative transport theory and formulate the problem under study. In section 3, the MRRF in the slab geometry is developed. In section 4, we describe the numerical aspects of solving the boundary-value problem in the slab. In section 5, we calculate the specific intensity, energy density and current using the MRRF. Numerical results are reported in section 6, where we compare computations using the MRRF with the diffusion approximation and Monte Carlo simulations. Our conclusions are presented in section 7.

2. Radiative transport in the slab geometry

Consider a slab of width L with boundaries on the planes $z = 0$ and $z = L$. The specific intensity $I(\mathbf{r}, \hat{\mathbf{s}})$ inside the slab is a function of position $\mathbf{r} = (\boldsymbol{\rho}, z)$ and the direction of propagation specified by the unit vector $\hat{\mathbf{s}}$. The specific intensity obeys the RTE:

$$\hat{\mathbf{s}} \cdot \nabla I(\mathbf{r}, \hat{\mathbf{s}}) + \mu_{\mathrm{t}} I(\mathbf{r}, \hat{\mathbf{s}}) = \mu_{\mathrm{s}} \int \mathrm{d}^2 s' A(\hat{\mathbf{s}}, \hat{\mathbf{s}}') I(\mathbf{r}, \hat{\mathbf{s}}'), \tag{1}$$

where μ_{a} and μ_{s} are the absorption and the scattering coefficients respectively, and $\mu_{\mathrm{t}} = \mu_{\mathrm{a}} + \mu_{\mathrm{s}}$ is the extinction coefficient. We consider a homogeneous medium and assume that the quantities μ_{a}, μ_{s} and the phase function $A(\hat{\mathbf{s}}, \hat{\mathbf{s}}')$ are independent of position. We also assume that the medium is isotropic on average, so that $A(\hat{\mathbf{s}}, \hat{\mathbf{s}}')$ is a function of $\hat{\mathbf{s}} \cdot \hat{\mathbf{s}}'$ only; it is normalized by the condition $\int \mathrm{d}^2 s' A(\hat{\mathbf{s}}, \hat{\mathbf{s}}') = 1$ for all $\hat{\mathbf{s}}$. We will utilize the above property to expand the phase function as

$$A(\hat{\mathbf{s}}, \hat{\mathbf{s}}') = \sum_{lm} A_l Y_{lm}(\hat{\mathbf{s}}) Y_{lm}^*(\hat{\mathbf{s}}'). \tag{2}$$

Here $A_0 = 1$ and $A_1 = \int \mathrm{d}^2 s' \, \hat{\mathbf{s}} \cdot \hat{\mathbf{s}}' A(\hat{\mathbf{s}}, \hat{\mathbf{s}}') \leqslant 1$ is the scattering asymmetry parameter. For the higher moments, we have $A_l < 1$ ($l = 2, 3, \ldots$). Note that isotropy of space is not equivalent to isotropy of scattering; the latter implies that $A(\hat{\mathbf{s}}, \hat{\mathbf{s}}') = 1/(4\pi)$, and correspondingly, $A_1 = 0$. We also utilize below a set of constants σ_l defined by

$$\sigma_l = \mu_{\mathrm{a}} + \mu_{\mathrm{s}}(1 - A_l). \tag{3}$$

Note that $\sigma_1 = 1/\ell^*$ is the inverse transport mean free path. We assume that $\mu_a > 0$ throughout the paper. However, we can consider the purely scattering case by taking the limit of $\mu_a \to 0$.

Suppose that a narrow collimated incident beam enters the slab from the vacuum at the interface $z = 0$ at the point $\boldsymbol{\rho} = \boldsymbol{\rho}_0$ and in the direction $\hat{\mathbf{s}}_0$. The specific intensity of the incident wave at the plane of incidence is

$$I_{\text{inc}}(\boldsymbol{\rho}, \hat{\mathbf{s}}) = I_0 \delta \left(\boldsymbol{\rho} - \boldsymbol{\rho}_0 \right) \delta \left(\hat{\mathbf{s}} - \hat{\mathbf{s}}_0 \right), \tag{4}$$

where I_0 is a constant. The specific intensity satisfies the boundary conditions

$$I(\boldsymbol{\rho}, z = 0, \hat{\mathbf{s}}) = I_{\text{inc}}(\boldsymbol{\rho}, \hat{\mathbf{s}}) \qquad \hat{\mathbf{s}} \cdot \hat{\mathbf{z}} > 0, \tag{5}$$

$$I(\boldsymbol{\rho}, z = L, \hat{\mathbf{s}}) = 0 \qquad \hat{\mathbf{s}} \cdot \hat{\mathbf{z}} < 0. \tag{6}$$

3. Method of rotated reference frames

Following [15], the solution to the RTE with the boundary conditions (5) and (6) will be constructed as a superposition of plane-wave modes:

$$I(\mathbf{r}, \hat{\mathbf{s}}) = \sum_{\mathbf{k}} F_{\mathbf{k}} I_{\mathbf{k}}(\mathbf{r}, \hat{\mathbf{s}}). \tag{7}$$

Here, the coefficients $F_{\mathbf{k}}$ are to be determined from the boundary conditions and the modes $I_{\mathbf{k}}(\mathbf{r}, \hat{\mathbf{s}})$ are of the form

$$I_{\mathbf{k}}(\mathbf{r}, \hat{\mathbf{s}}) = \sum_{lm} C_{lm} Y_{lm}(\hat{\mathbf{s}}; \hat{\mathbf{k}}) \exp(-\mathbf{k} \cdot \mathbf{r}), \tag{8}$$

where C_{lm} are constants and $Y_{lm}(\hat{\mathbf{s}}; \hat{\mathbf{k}})$ are spherical functions defined in the rotated reference frame whose z-axis coincides with the direction of the unit vector $\hat{\mathbf{k}} = \mathbf{k}/k, k = \sqrt{\mathbf{k} \cdot \mathbf{k}}$. Here and everywhere below the branch of a square root of an arbitrary complex number z is determined by applying the condition $0 \leqslant \arg\left(\sqrt{z}\right) < \pi$.

The rotated reference frame is uniquely defined by the three Euler angles α, β, γ. The converse, however, is not true: there is more than one set of Euler angles that correspond to the same rotation. Therefore, we set the third Euler angle γ to zero. Any rotation of the reference frame is then uniquely defined by the two remaining angles α and β, and vice versa. The functions $Y_{lm}(\hat{\mathbf{s}}; \hat{\mathbf{k}})$ are related to the spherical functions defined in the laboratory frame, $Y_{lm}(\hat{\mathbf{s}})$, by

$$Y_{lm}(\hat{\mathbf{s}}; \hat{\mathbf{k}}) = \sum_{lm'} D^l_{m'm}(\varphi_{\hat{\mathbf{k}}}, \theta_{\hat{\mathbf{k}}}, 0) Y_{lm'}(\hat{\mathbf{s}}), \tag{9}$$

where $D^l_{m'm}(\alpha, \beta, \gamma)$ are the Wigner D-functions [20] and $\varphi_{\hat{\mathbf{k}}}, \theta_{\hat{\mathbf{k}}}$ are the polar and azimuthal angles of $\hat{\mathbf{k}}$ in the laboratory frame. The Wigner D-functions are given in terms of the Wigner d-functions as $D^l_{m'm}(\alpha, \beta, \gamma) = \exp(-im'\alpha) d^l_{m'm}(\beta) \exp(-im\gamma)$.

Substitution of (8) into (1) results in the following generalized eigenproblem:

$$k \sum_{l'm'} R^{l'm'}_{lm} C_{l'm'} = \sigma_l C_{lm}, \tag{10}$$

where σ_l is defined in (3) and

$$R^{l'm'}_{lm} = \int d^2s \, \hat{\mathbf{s}} \cdot \hat{\mathbf{k}} Y^*_{lm}(\hat{\mathbf{s}}; \hat{\mathbf{k}}) Y_{l'm'}(\hat{\mathbf{s}}; \hat{\mathbf{k}})$$

$$= \int d^2s \, \hat{\mathbf{s}} \cdot \hat{\mathbf{z}} Y^*_{lm}(\hat{\mathbf{s}}) Y_{l'm'}(\hat{\mathbf{s}}). \tag{11}$$

Note that $R_{lm}^{l'm'} = 0$ if $m \neq m'$. The generalized eigenproblem (10) can be transformed into a standard eigenproblem. To this end, we define the diagonal matrix $S_{lm}^{l'm'} = \delta_{mm'}\delta_{ll'}\sqrt{\sigma_l}$. Since $A_l \leqslant 1$ and correspondingly $\sigma_l > 0$, the matrix S is invertible. It is then easy to see that (10) is equivalent to the equation $kW|\psi\rangle = |\psi\rangle$, where $W = S^{-1}RS^{-1}$ and $|\psi\rangle = S|C\rangle$.

Since the matrix R is symmetric and block tridiagonal, so is W. We will denote the individual blocks of W by $B(M)$ ($M = 0, \pm 1, \pm 2, \ldots$); each block can be diagonalized separately:

$$B_l^{l'}(M) = \beta_l(M)\delta_{l',l-1} + \beta_{l+1}(M)\delta_{l',l+1}, \tag{12}$$

$$\beta_l(M) = \sqrt{\frac{l^2 - M^2}{(4l^2 - 1)\sigma_{l-1}\sigma_l}}, \tag{13}$$

$$l, l' = |M|, |M| + 1, \ldots.$$

The eigenproblem is then reduced to computing the eigenvalues and eigenvectors of the infinite set of tridiagonal matrices $B(M)$, denoted here by $\lambda_n(M)$ and $|\phi_n(M)\rangle$, respectively. Here the index n labels the eigenvalues, which can belong to the continuous spectrum, in which case n should be viewed as a continuous variable. We will also use a composite index $\mu = (M, n)$ which runs over the following set: $\mu \in \{(M, n)|\lambda_n(M) > 0\}$, since only the positive eigenvalues and corresponding eigenvectors will eventually enter the solution.

From the eigenproblem (10), we see that the wave vector $\mathbf{k}$ must satisfy $k = \sqrt{\mathbf{k} \cdot \mathbf{k}} = 1/\lambda_\mu$. The variable k can also take negative values because $-\lambda_\mu$ is also an eigenvalue if λ_μ is an eigenvalue. This fact is taken into account in (15), where we consider both signs. If a matrix $B(M)$ is truncated so that its dimension is odd, it has one zero eigenvalue. The corresponding mode decays infinitely fast into the medium and can be safely excluded. This problem can be avoided by truncating $B(M)$ so that its dimension is even. We can, therefore, write $\mathbf{k} = \hat{\mathbf{k}}/\lambda_\mu$, where $\hat{\mathbf{k}}$ is an arbitrary unit vector. Thus, instead of a general three-dimensional vector $\mathbf{k}$, the modes can be labeled by the unit vector $\hat{\mathbf{k}}$ and the index μ. In terms of the spherical functions defined in the laboratory frame, $Y_{lm}(\hat{\mathbf{s}})$, the modes can be written as

$$I_{\hat{\mathbf{k}},\mu}(\mathbf{r}, \hat{\mathbf{s}}) = \exp\left(-\frac{\hat{\mathbf{k}} \cdot \mathbf{r}}{\lambda_\mu}\right) \sum_{lm} Y_{lm}(\hat{\mathbf{s}}) \frac{\exp(-im\phi_{\hat{\mathbf{k}}})}{\sqrt{\sigma_l}} \langle l|\phi_\mu\rangle d_{mM}^l(\theta_{\hat{\mathbf{k}}}), \tag{14}$$

where d_{mM}^l are the Wigner d-functions and $\theta_{\hat{\mathbf{k}}}, \phi_{\hat{\mathbf{k}}}$ are the polar and azimuthal angles of $\hat{\mathbf{k}}$.

In order to solve the boundary-value problem, the modes defined in (14) must be analytically continued. The analytical continuation will give rise to *evanescent* modes of the RTE. The wave vectors of such modes are of the form

$$\mathbf{k}_\pm = -i\mathbf{q} \pm Q_\mu(q)\hat{\mathbf{z}}, \tag{15}$$

where $\mathbf{q}$ is an arbitrary two-dimensional, purely real vector in the xy-plane and

$$Q_\mu(q) = \sqrt{q^2 + 1/\lambda_\mu^2}. \tag{16}$$

The above modes are labeled by the composite index $\mu = (M, n)$ and the two-dimensional vector $\mathbf{q}$.

The unit vector $\hat{\mathbf{k}}$ in (14) should also be analytically continued. This is accomplished by writing

$$\hat{\mathbf{k}} = \hat{\mathbf{k}}_\pm = \lambda_\mu\mathbf{k}_\pm = -iq\lambda_\mu\hat{\mathbf{q}} \pm Q_\mu(q)\lambda_\mu\hat{\mathbf{z}}, \tag{17}$$

where the choice of the plus or minus sign corresponds to the choice of sign in (15). It can be verified that $\hat{\mathbf{k}} \cdot \hat{\mathbf{k}} = 1$. The cosine and sine of the polar angle $\theta_{\hat{\mathbf{k}}}$ are defined by the relations

$$\cos\theta_{\hat{\mathbf{k}}_\pm} = \hat{\mathbf{k}}_\pm \cdot \hat{\mathbf{z}} = \pm\sqrt{1 + (q\lambda_\mu)^2}, \qquad \sin\theta_{\hat{\mathbf{k}}_\pm} = \sqrt{1 - \cos^2\theta_{\hat{\mathbf{k}}_\pm}} = iq\lambda_\mu, \tag{18}$$

where we have used the square root convention stated above. The azimuthal angle $\phi_{\hat{\mathbf{k}}_\pm}$ is obtained as

$$\phi_{\hat{\mathbf{k}}_\pm} = \phi_{\hat{\mathbf{q}}} + \pi, \tag{19}$$

where $\phi_{\hat{\mathbf{q}}}$ is the polar angle of the real vector $\mathbf{q}$ in the xy-plane.

Since $\hat{\mathbf{k}}$ is a function of $q\lambda_\mu$ (defined by (16) and (17)), we write $\theta_{\hat{\mathbf{k}}} = \mathrm{i}\tau(q\lambda_\mu)$ where $\tau(x)$ is a function

$$\cos[\mathrm{i}\tau(x)] = \sqrt{1+x^2}, \qquad \sin[\mathrm{i}\tau(x)] = \mathrm{i}x. \tag{20}$$

Similarly, the analytically continued Wigner d-functions can be expressed as

$$d_{mM}^l(\theta_{\hat{\mathbf{k}}_+}) = d_{mM}^l[\mathrm{i}\tau(q\lambda_\mu)], \tag{21}$$

$$d_{mM}^l(\theta_{\hat{\mathbf{k}}_-}) = d_{mM}^l(\pi - \theta_{\hat{\mathbf{k}}_+}) = (-1)^{l+m} d_{m,-M}^l[\mathrm{i}\tau(q\lambda_\mu)]. \tag{22}$$

In numerical simulations, we compute $d_{mM}^l[\mathrm{i}\tau(x)]$ by recursion as described in section 6.2. In appendix A, these functions are given in terms of Jacobi polynomials and analytically continued to complex arguments. In numerical simulations, we computed the Wigner functions iteratively by utilizing the so-called Wigner d-matrix pyramid, as explained in appendix B.

We now insert (15) into (14) and obtain the following two evanescent modes:

$$I_{\mathbf{q}\mu}^{(+)}(\mathbf{r},\hat{\mathbf{s}}) = \exp[\mathrm{i}\mathbf{q}\cdot\boldsymbol{\rho} - Q_\mu(q)z] \sum_{l=0}^{\infty} \sum_{m=-l}^{l} Y_{lm}(\hat{\mathbf{s}})$$
$$\times \frac{\exp[-\mathrm{i}m(\phi_\mathbf{q}+\pi)]}{\sqrt{\sigma_l}} \langle l|\phi_\mu\rangle d_{mM}^l[\mathrm{i}\tau(q\lambda_\mu)], \tag{23}$$

$$I_{\mathbf{q}\mu}^{(-)}(\mathbf{r},\hat{\mathbf{s}}) = \exp[\mathrm{i}\mathbf{q}\cdot\boldsymbol{\rho} + Q_\mu(q)z] \sum_{l=0}^{\infty} \sum_{m=-l}^{l} Y_{lm}(\hat{\mathbf{s}})(-1)^{l+m}$$
$$\times \frac{\exp[-\mathrm{i}m(\phi_\mathbf{q}+\pi)]}{\sqrt{\sigma_l}} \langle l|\phi_\mu\rangle d_{m,-M}^l[\mathrm{i}\tau(q\lambda_\mu)]. \tag{24}$$

As can be seen, $I_{\mathbf{q}\mu}^{(+)}$ decays exponentially in the positive z-direction, while $I_{\mathbf{q}\mu}^{(-)}$ decays in the negative z-direction. The completeness of these modes is shown in [15]; the Green's function in the infinite medium is spanned by $I_{\mathbf{q}\mu}^{(+)}$ and $I_{\mathbf{q}\mu}^{(-)}$.

4. Boundary-value problem

The solution to the boundary-value problem in the slab geometry contains only evanescent modes given in (23) and (24). Therefore, expansion (7) can be written as

$$I(\mathbf{r},\hat{\mathbf{s}}) = \sum_\mu \int \frac{\mathrm{d}^2 q}{(2\pi)^2} \left[F_{\mathbf{q}\mu}^{(+)} I_{\mathbf{q}\mu}^{(+)}(\mathbf{r},\hat{\mathbf{s}}) + F_{\mathbf{q}\mu}^{(-)} I_{\mathbf{q}\mu}^{(-)}(\mathbf{r},\hat{\mathbf{s}}) \right]. \tag{25}$$

To obtain the coefficients $F_{\mathbf{q}\mu}^{(\pm)}$, we rewrite the boundary conditions as

$$I(\boldsymbol{\rho}, z=0, \hat{\mathbf{s}}) = \Theta(\hat{\mathbf{s}}\cdot\hat{\mathbf{z}}) I_0 \delta(\boldsymbol{\rho}-\boldsymbol{\rho}_0) \sum_{lm} Y_{lm}^*(\hat{\mathbf{s}}_0) Y_{lm}(\hat{\mathbf{s}})$$
$$+ \Theta(-\hat{\mathbf{s}}\cdot\hat{\mathbf{z}}) I(\boldsymbol{\rho}, z=0, \hat{\mathbf{s}}), \tag{26}$$

$$I(\boldsymbol{\rho}, z=L, \hat{\mathbf{s}}) = \Theta(\hat{\mathbf{s}}\cdot\hat{\mathbf{z}}) I(\boldsymbol{\rho}, z=L, \hat{\mathbf{s}}), \tag{27}$$

where $\Theta(\cdot)$ denotes the Heaviside step function and we have used the identity $\delta(\hat{\mathbf{s}} - \hat{\mathbf{s}}_0) = \sum_{lm} Y^*_{lm}(\hat{\mathbf{s}}_0) Y_{lm}(\hat{\mathbf{s}})$. We then act on (26) and (27) with $\int d^2 s\, Y^*_{l'm'}(\hat{\mathbf{s}}) \int d^2\rho\, e^{-i\mathbf{q}\cdot\rho}$, perform the integration and obtain

$$\sum_\mu \sum_l \mathcal{B}^{m'}_{l'l} \frac{e^{-im'(\phi_\mathbf{q}+\pi)}}{\sqrt{\sigma_l}} \langle l|\phi_\mu\rangle \left[F^{(+)}_{\mathbf{q}\mu} d^l_{m'M}[i\tau(q\lambda_\mu)] + F^{(-)}_{\mathbf{q}\mu}(-1)^{l+m'} d^l_{m'-M}[i\tau(q\lambda_\mu)] \right]$$

$$= I_0 e^{-i\mathbf{q}\cdot\rho_0} \sum_l \mathcal{B}^{m'}_{l'l} Y^*_{lm'}(\hat{\mathbf{s}}_0), \tag{28}$$

$$\sum_\mu \sum_l \mathcal{B}^{m'}_{l'l}(-1)^{l+l'} \frac{e^{-im'(\phi_\mathbf{q}+\pi)}}{\sqrt{\sigma_l}} \langle l|\phi_\mu\rangle$$

$$\times \left[F^{(+)}_{\mathbf{q}\mu} e^{-Q_\mu(q)L} d^l_{m'M}[i\tau(q\lambda_\mu)] + F^{(-)}_{\mathbf{q}\mu} e^{Q_\mu(q)L}(-1)^{l+m'} d^l_{m'-M}[i\tau(q\lambda_\mu)] \right]$$

$$= 0. \tag{29}$$

Here $\mathcal{B}^m_{ll'}$ is defined by the following 'half-range' integrals:

$$\int_{\hat{\mathbf{s}}\cdot\hat{\mathbf{z}}>0} d^2 s\, Y^*_{l'm'}(\hat{\mathbf{s}}) Y_{lm}(\hat{\mathbf{s}}) = \delta_{mm'} \mathcal{B}^m_{ll'}, \tag{30}$$

$$\int_{\hat{\mathbf{s}}\cdot\hat{\mathbf{z}}<0} d^2 s\, Y^*_{l'm'}(\hat{\mathbf{s}}) Y_{lm}(\hat{\mathbf{s}}) = \delta_{mm'}(-1)^{l+l'} \mathcal{B}^m_{ll'}, \tag{31}$$

$$\mathcal{B}^m_{ll'} = \frac{1}{2} \left[\frac{(2l+1)(2l'+1)(l-m)!(l'-m)!}{(l+m)!(l'+m)!} \right]^{1/2} \int_0^1 dx\, P^m_l(x) P^m_{l'}(x). \tag{32}$$

Note that $\mathcal{B}^m_{ll'} = \mathcal{B}^{-m}_{ll'}$, and $\mathcal{B}^m_{ll'} = \frac{1}{2}\delta_{ll'}$ if l and l' have the same parity. The coefficients $F^{(\pm)}_{\mathbf{q}\mu}$ are obtained by solving equations (28) and (29) numerically.

Below, we report computations for the case of normal incidence with $\hat{\mathbf{s}}_0 = \hat{\mathbf{z}}$. In this situation, we obtain the simpler result

$$F^{(+)}_{\mathbf{q}\mu} = I_0 f^{(+)}_\mu(q) e^{-i\mathbf{q}\cdot\rho_0}, \tag{33}$$

$$F^{(-)}_{\mathbf{q}\mu} = I_0 f^{(-)}_\mu(q) e^{-i\mathbf{q}\cdot\rho_0} e^{-Q_\mu(q)L}, \tag{34}$$

where $f^{(\pm)}_\mu(q)$ satisfy

$$\sum_{\mu,l} \mathcal{B}^{m'}_{l'l} \frac{1}{\sqrt{\sigma_l}} \langle l|\phi_\mu\rangle \left[f^{(+)}_\mu(q) d^l_{m'M}[i\tau(q\lambda_\mu)] + f^{(-)}_\mu(q) e^{-Q_\mu(q)L}(-1)^{l+m'} d^l_{m'-M}[i\tau(q\lambda_\mu)] \right]$$

$$= \delta_{m'0} \sum_l \mathcal{B}^{m'}_{l'l} \sqrt{\frac{2l+1}{4\pi}}, \tag{35}$$

$$\sum_{\mu,l} \mathcal{B}^{m'}_{l'l} \frac{(-1)^{l+l'}}{\sqrt{\sigma_l}} \langle l|\phi_\mu\rangle \left[f^{(+)}_\mu(q) e^{-Q_\mu(q)L} d^l_{m'M}[i\tau(q\lambda_\mu)] + f^{(-)}_\mu(q)(-1)^{l+m'} d^l_{m'-M}[i\tau(q\lambda_\mu)] \right]$$

$$= 0. \tag{36}$$

Note that in the case of oblique incidence ($\hat{\mathbf{s}}_0 \neq \hat{\mathbf{z}}$), the coefficients $f^{(+)}_\mu$ and $f^{(-)}_\mu$ depend on the full two-dimensional vector $\mathbf{q}$, as does the matrix $\mathcal{M}$ defined below. We then must solve for $f^{(+)}_\mu$ and $f^{(-)}_\mu$ for each value of $\mathbf{q}$.

Equations (35) and (36) are invariant with respect to the substitution $m' \to -m'$. Therefore, we obtain

$$f_{-Mn}(q) = (-1)^M f_{Mn}(q), \tag{37}$$

where we have expanded the composite index μ: $\mu = (M, n)$. Thus, it is sufficient to use only the equations with $m' \geqslant 0$ and the sums over M run only in $M \geqslant 0$.

Equations (35) and (36) can be written in matrix form as

$$\begin{pmatrix} \mathcal{M}^{(++)}(q) \mathcal{M}^{(+-)}(q) \\ \mathcal{M}^{(-+)}(q) \mathcal{M}^{(--)}(q) \end{pmatrix} \begin{pmatrix} f^{(+)}(q) \\ f^{(-)}(q) \end{pmatrix} = \begin{pmatrix} v^{(+)} \\ v^{(-)} \end{pmatrix}. \tag{38}$$

Here

$$v^{(+)}_{l'm'} = \delta_{m'0} \sum_l \mathcal{B}^0_{l'l} \sqrt{\frac{2l+1}{4\pi}}, \qquad v^{(-)}_{l'm'} \equiv 0, \tag{39}$$

and

$$\mathcal{M}^{(++)}_{l'm',Mn} = \sum_l c_{ll'm',Mn}, \tag{40}$$

$$\mathcal{M}^{(+-)}_{l'm',Mn} = e^{-Q_\mu(q)L}(-1)^{M+m'} \sum_l (-1)^l c_{ll'm',Mn}, \tag{41}$$

$$\mathcal{M}^{(-+)}_{l'm',Mn} = e^{-Q_\mu(q)L} \sum_l (-1)^{l+l'} c_{ll'm',Mn}, \tag{42}$$

$$\mathcal{M}^{(--)}_{l'm',Mn} = (-1)^{l'+m'+M} \sum_l c_{ll'm',Mn}, \tag{43}$$

$$c_{ll'm',Mn} = \mathcal{B}^{m'}_{l'l} \frac{1}{\sqrt{\sigma_l}} \langle l|\phi_\mu\rangle \left\{ d^l_{m'M}[i\tau(q\lambda_\mu)] + (1-\delta_{M0})(-1)^M d^l_{m'-M}[i\tau(q\lambda_\mu)] \right\}. \tag{44}$$

The system $\mathcal{M}|f\rangle = |v\rangle$ given in (38) is an infinite set of linear equations which must be truncated in a numerical implementation. The truncated set contains approximately twice as many equations as unknowns (see step 3 in section 6.2). However, approximately half of these equations are not linearly independent. In the infinite system limit, a solution exists and is unique. However, in the truncated set, this may not be the case if the truncation is not done carefully. Although a rigorous method exists to select only linearly independent equations (which will be reported elsewhere), in this paper the solution to (38) is obtained by computing the SVD pseudo-inverse [21–23] of $\mathcal{M}$.

5. Specific intensity, density and current

From (23), (24) and (25), it follows that the specific intensity can be written in the form

$$I(\mathbf{r}, \hat{\mathbf{s}}) = \frac{I_0}{2\pi} \sum_{lm} \frac{(-i)^m}{\sqrt{\sigma_l}} e^{-im\phi_{\rho-\rho_0}} Y_{lm}(\hat{\mathbf{s}}) K_{lm}(|\boldsymbol{\rho} - \boldsymbol{\rho}_0|, z), \tag{45}$$

where $\phi_{\rho-\rho_0}$ is the polar angle of the two-dimensional vector $\boldsymbol{\rho} - \boldsymbol{\rho}_0$ (it is often convenient to place the source at the origin so that $\boldsymbol{\rho}_0 = 0$) and

$$K_{lm}(|\boldsymbol{\rho} - \boldsymbol{\rho}_0|, z) = \int dq\, q\, J_m(q|\boldsymbol{\rho} - \boldsymbol{\rho}_0|) \sum_{M \geqslant 0, n} \langle l|\phi_\mu\rangle$$
$$\times \left[e^{-Q_\mu(q)z} f^{(+)}_{Mn}(q) + (-1)^{l+m+M} e^{-Q_\mu(q)(L-z)} f^{(-)}_{Mn}(q) \right]$$
$$\times \left[d^l_{mM}[i\tau(q\lambda_\mu)] + (1-\delta_{M0})(-1)^M d^l_{m,-M}[i\tau(q\lambda_\mu)] \right], \tag{46}$$

with $J_m(z)$ being the Bessel functions of the first kind. Since $K_{l,-m}(|\boldsymbol{\rho} - \boldsymbol{\rho}_0|, z) = K_{l,m}(|\boldsymbol{\rho} - \boldsymbol{\rho}_0|, z)$, we obtain

$$
\begin{aligned}
I(\mathbf{r}, \hat{\mathbf{s}}) = \frac{I_0}{2\pi} &\sum_{l=0}^{\infty} \sum_{m=0}^{l} \frac{(-\mathrm{i})^m}{\sqrt{\sigma_l}} K_{lm}(|\boldsymbol{\rho} - \boldsymbol{\rho}_0|, z) \\
&\times \left[\mathrm{e}^{-\mathrm{i}m\phi_{\rho-\rho_0}} Y_{lm}(\hat{\mathbf{s}}) + (1 - \delta_{m0}) \mathrm{e}^{\mathrm{i}m\phi_{\rho-\rho_0}} Y_{lm}^*(\hat{\mathbf{s}}) \right].
\end{aligned}
\tag{47}
$$

The density u and the current $\mathbf{J}$ of electromagnetic energy are defined as follows:

$$
u(\mathbf{r}) = \frac{1}{c} \int \mathrm{d}^2 s I(\mathbf{r}, \hat{\mathbf{s}}) = \left(\frac{I_0}{c} \right) \frac{K_{00}(|\boldsymbol{\rho} - \boldsymbol{\rho}_0|, z)}{\sqrt{\pi \sigma_0}},
\tag{48}
$$

$$
\mathbf{J}(\mathbf{r}) = \int \mathrm{d}^2 s \hat{\mathbf{s}} I(\mathbf{r}, \hat{\mathbf{s}}) = \begin{pmatrix} J_\rho \cos \phi_{\rho-\rho_0} \\ J_\rho \sin \phi_{\rho-\rho_0} \\ J_z \end{pmatrix},
\tag{49}
$$

where c is the average speed of light in the medium and

$$
J_z = \frac{I_0}{\sqrt{3\pi \sigma_1}} K_{10}(|\boldsymbol{\rho} - \boldsymbol{\rho}_0|, z), \qquad J_\rho = \mathrm{i} I_0 \sqrt{\frac{2}{3\pi \sigma_1}} K_{11}(|\boldsymbol{\rho} - \boldsymbol{\rho}_0|, z).
\tag{50}
$$

Note that we can readily obtain the specific intensity, density and current in the half-space geometry by taking the limit of $L \to \infty$.

6. Numerical results

6.1. Parameters

We adopt the Henyey–Greenstein model for the phase function [25]. Here the expansion coefficients A_l in (2) are given by $A_l = g^l$, where $0 \leqslant g < 1$ is the scattering asymmetry parameter. We use the numerical value $g = 0.9$ which corresponds to highly forward-peaked scattering, characteristic of biological tissues in the near-IR spectral range [1].

The absorption and the reduced scattering coefficients are taken to be $\mu_a = 0.05 \, \text{cm}^{-1}$ and $\mu_s' = \mu_s(1 - g) = 10 \, \text{cm}^{-1}$. This corresponds to the transport mean free path $\ell^* = 1/(\mu_a + \mu_s') = 0.099\,50 \, \text{cm}$.

Five different values of the slab width, L, are used: $L = 50\ell^*, 10\ell^*, 7\ell^*, 5\ell^*$ and $3\ell^*$.

For the case of normal incidence, the specific intensity is axially symmetric with respect to the incident beam. Therefore, without loss of generality, we take $\boldsymbol{\rho}_0 = \mathbf{0}$ and $\phi_{\rho-\rho_0} = 0$. Thus, the position of the observation point is specified by two parameters, z and ρ.

The indices l and l' in $B_l^{l'}(M)$ (12) and the summation over l in (45) will be truncated by $l, l' \leqslant l_{max}$. In most cases, $l_{max} \lesssim 10$ will prove to be sufficient.

The integral over q is computed numerically by the Simpson rule in a finite interval $q \in [0, q_{max}]$ with N_q discretization points.

6.2. The numerical procedure

The numerical procedure is divided into the following four steps.

Step 1: Compute the matrix $\mathcal{B}_{ll'}^{m'}$.
Step 2: Compute λ_μ and $|\phi_\mu\rangle$ by diagonalizing the tridiagonal matrices $B(M)(M = 0, 1, \ldots, l_{max})$. We need $l_{max}(l_{max} + 2)/4$ or $(l_{max} + 1)^2/4$ positive eigenvalues, depending on whether l_{max} is even or odd.
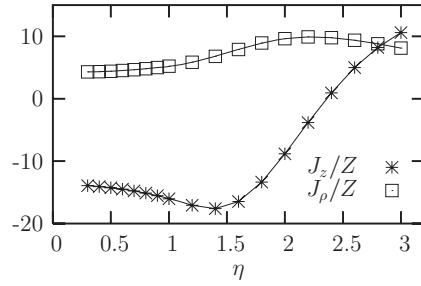
Figure 1. Convergence of the current components J_z and J_ρ with η. The point of observation is located at the plane of incidence ($z = 0$, $\rho = 5\ell^*$). Other parameters: $l_{max} = 9$ and $L = 10\ell^*$. Normalization factor: $Z = 10^4 I_0/(\ell^*)^2$.

Step 3: Compute K_{lm} for l ($= 0, \ldots, l_{max}$) and m ($= 0, \ldots, l$). To this end, we compute the matrix $\mathcal{M}$ by calculating $d^l_{mM}[i\tau(q_i\lambda_\mu)]$ for q_i ($i = 0, \ldots, N_q$). The size of $\mathcal{M}$ is $(l_{max} + 1)(l_{max} + 2) \times l_{max}(l_{max} + 2)/2$ for even l_{max} and $(l_{max} + 1)(l_{max} + 2) \times (l_{max} + 1)^2/2$ for odd l_{max}. We then solve $\mathcal{M}|f\rangle = |v\rangle$ by SVD pseudo-inverse. After that, we obtain K_{lm} by numerical integration.

Step 4: The density $u(\mathbf{r})$, the current $\mathbf{J}(\mathbf{r})$ and the specific intensity $I(\mathbf{r}, \hat{\mathbf{s}})$ are computed according to (48), (49) and (45), using the coefficients K_{lm} obtained in the previous step.

A few comments are needed regarding step 3. First, we calculate the analytically continued Wigner d-functions $d^l_{mM}[i\tau(x)]$ according to the Wigner d-matrix pyramid for $d^l_{mM}(\theta)$ [26–28]; the algorithm is described in appendix B. Second, numerical calculation of the coefficients $f^{(\pm)}_\mu(q)$ by solving the system $\mathcal{M}|f\rangle = |v\rangle$ can be unstable for large values of q. However, calculation of the specific intensity for small values of z, such that $z \lesssim \ell^*$, requires relatively large values of q_{max}. In such cases, we introduce a Gaussian function to regularize the integral in (46). More specifically, we replace the integral in (46) by

$$\int_0^\infty \mathrm{d}q\, f(q) = \lim_{\eta \to 0} \int_0^\infty \mathrm{d}q \exp\left[-\frac{\eta^2}{2}q^2\right] f(q). \tag{51}$$

Here η is a small regularization parameter and $f(q)$ is given in (46). We can estimate the value of η which is required for fast convergence as $\eta \sim \sqrt{2(1 - q_{max}z)}/q_{max}$. For $z > 1/q_{max}$, we can take $\eta = 0$. Note that this technique is frequently used for evaluation of oscillatory integrals [24].

Numerical convergence of the current components J_z and J_ρ with η computed at the incidence face of the slab ($z = 0$, $\rho = 5\ell^*$) is illustrated in figure 1. Here, J_z and J_ρ are plotted as functions of η for $l_{max} = 9$ in a slab with $L = 10\ell^*$. It can be seen that convergence is reached for $\eta < 0.5$.

In step 4, we need to compute the spherical functions. To do so, we make use of the relation

$$Y_{lm}(\theta_\mathbf{s}, \phi_\mathbf{s}) = \sqrt{\frac{2l + 1}{4\pi}} \exp(im\phi_\mathbf{s})\, d^l_{m0}(\theta_\mathbf{s}), \tag{52}$$

where the Wigner d-functions $d^l_{m0}(\theta_\mathbf{s})$ are calculated from the Wigner d-matrix pyramid.

Convergence of the current components J_z and J_ρ with l_{max} is illustrated in figure 2. Here the observation points are located in the following points: $(z, \rho) = (0, 5\ell^*)$, $(5\ell^*, 5\ell^*)$ and $(10\ell^*, 5\ell^*)$; the slab width is $L = 10\ell^*$. We use $\eta = 0.4$ when the point of observation is
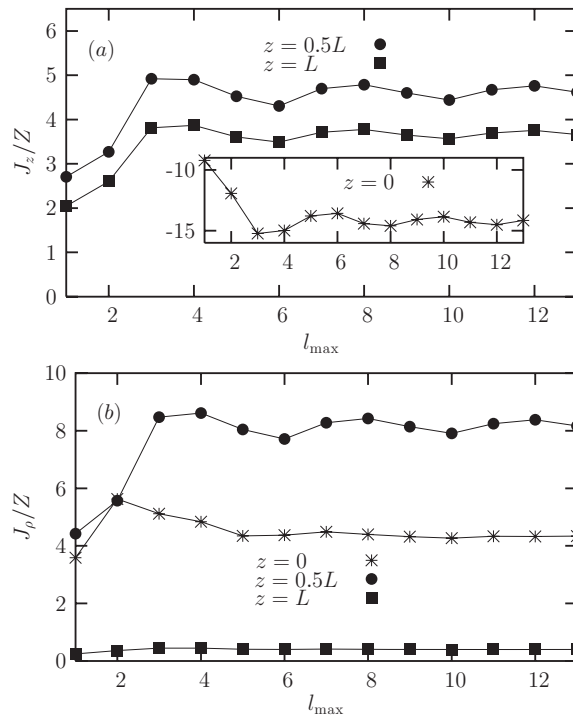
Figure 2. Current components J_z (*a*) and J_ρ (*b*) as functions of l_{max} for the following three points of observation: $(\rho, z) = (5\ell^*, 0)$, $(5\ell^*, 5\ell^*)$ and $(5\ell^*, 10\ell^*)$. The slab width is $L = 10\ell^*$. Normalization factor: $Z = 10^4 I_0/(\ell^*)^2$.
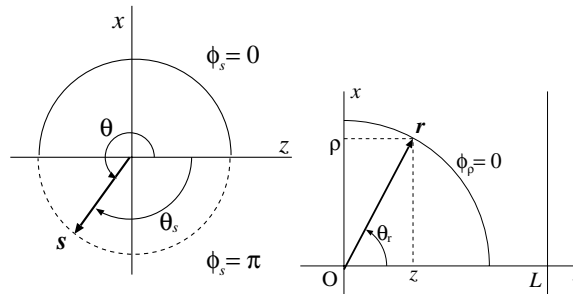

Figure 3. (Left) the angles θ, θ_s and ϕ_s. (Right) the angles θ_r and ϕ_ρ.

located at $(z, \rho) = (0, 5\ell^*)$. In other cases, regularization of the q-integral is not needed and we set $\eta = 0$. It can be seen that both J_z and J_ρ converge for $l_{max} > 4$.

6.3. Specific intensity

In figure 4, the specific intensity is plotted as a function of the polar angle of the vector $\hat{s}$, θ. The angle $\theta (0 \leqslant \theta < 2\pi)$ is illustrated in figure 3.
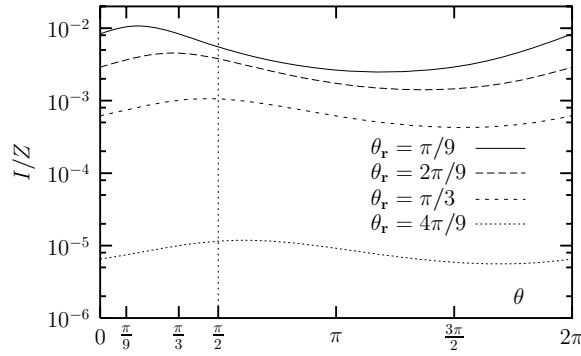
10

Figure 4. Specific intensity $I(\mathbf{r}, \hat{\mathbf{s}})$ computed at $z = 2\ell^*$ and plotted as a function of θ with $l_{\max} = 9$ and $\eta = 0.4$. Normalization factor: $Z = I_0/(\ell^*)^2$.
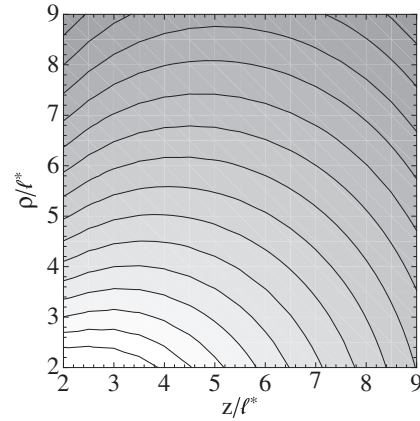

Figure 5. Specific intensity $I(\mathbf{r}, \hat{\mathbf{s}} = \hat{\mathbf{z}})$ as a function of two variables: ρ and z. Logarithmic color scale is used. The slab width is $L = 10\ell^*$. The source is located at $(z, \rho) = (0, 0)$. We use $l_{\max} = 9$, and $\eta \simeq 0.5$ for $z < 2.5$; otherwise, $\eta = 0$.

We see that the maxima of $I(\mathbf{r}, \hat{\mathbf{s}})$ are in the direction of the positive z-axis for $\theta_{\mathbf{r}} = \pi/9, 2\pi/9$ and $\pi/3$, whereas the peak is in the direction of the negative z-axis for $\theta_{\mathbf{r}} = 4\pi/9$.

A contour plot of $I(\mathbf{r}, \hat{\mathbf{s}} = \hat{\mathbf{z}})$ as a function of z and ρ is shown in figure 5. Here $I(\mathbf{r}, \hat{\mathbf{s}} = \hat{\mathbf{z}})$ was calculated with $l_{\max} = 9$. A nonzero regularization parameter η ($\simeq 0.5$) was used for $z < 2.5\ell^*$.

6.4. Current

The diffusion equation is often used as an approximation to the RTE [6, 29]. In this section, we compare the current **J** computed using the MRRF to the respective quantity obtained in the diffusion approximation (DA). In the DA, the specific intensity is obtained by solving the diffusion equation with appropriate boundary conditions. Explicit analytical solutions in the slab geometry were obtained in [30]. In particular, for the current components, J_z and J_ρ (not

to be confused with the Bessel functions J_0 and J_1), we have

$$J_z = -I_0(1 - \ell^* \mu_a) \int \frac{q\,dq}{4\pi Q\ell^*} J_0(q|\boldsymbol{\rho} - \boldsymbol{\rho}_0|)$$
$$\times \frac{[1 + (Q\ell)^2]c'_-(z) - [1 - (Q\ell)^2]c'_+(z) + 2Q\ell s'_-(z)}{2Q\ell \cosh(QL) + [1 + (Q\ell)^2]\sinh(QL)}, \quad (53)$$

$$J_\rho = I_0(1 - \ell^* \mu_a) \int \frac{q\,dq}{4\pi Q\ell^*} J_1(q|\boldsymbol{\rho} - \boldsymbol{\rho}_0|)$$
$$\times \frac{[1 + (Q\ell)^2]c_-(z) - [1 - (Q\ell)^2]c_+(z) + 2Q\ell s_-(z)}{2Q\ell \cosh(QL) + [1 + (Q\ell)^2]\sinh(QL)}, \quad (54)$$

where

$$\ell = \frac{2}{3}\ell^*, \qquad Q = \sqrt{q^2 + \frac{3\mu_a}{\ell^*}}. \quad (55)$$

We note that $c'_+(z)$, $c'_-(z)$ and $s'_-(z)$ stand for the derivatives of $c_+(z)$, $c_-(z)$ and $s_-(z)$, respectively. The functions $c_+(z)$, $c_-(z)$ and $s_-(z)$ are given as follows:

$$c_+(z) = \int_0^L dz' \exp[-z'/\ell^*] \cosh[Q(L - |z + z'|)]$$
$$= \frac{\ell^*}{2(1 - Q\ell^*)}[e^{-QL} - e^{-L/\ell^*}]e^{Qz} + \frac{\ell^*}{2(1 + Q\ell^*)}[e^{QL} - e^{-L/\ell^*}]e^{-Qz}, \quad (56)$$

$$c_-(z) = \int_0^L dz' \exp[-z'/\ell^*] \cosh[Q(L - |z - z'|)]$$
$$= \frac{\ell^*}{2(1 - Q\ell^*)}[(e^{QL} - e^{-L/\ell^*})e^{-Qz} - (e^{QL} - e^{-QL})e^{-z/\ell^*}]$$
$$+ \frac{\ell^*}{2(1 + Q\ell^*)}[-(e^{-L/\ell^*} - e^{-QL})e^{Qz} + (e^{QL} - e^{-QL})e^{-z/\ell^*}], \quad (57)$$

and

$$s_-(z) = \int_0^L dz' \exp[-z'/\ell^*] \sinh[Q(L - |z - z'|)]$$
$$= \frac{\ell^*}{2(1 - Q\ell^*)}[(e^{QL} + e^{-L/\ell^*})e^{-Qz} - (e^{QL} + e^{-QL})e^{-z/\ell^*}]$$
$$+ \frac{\ell^*}{2(1 + Q\ell^*)}[-(e^{-L/\ell^*} + e^{-QL})e^{Qz} + (e^{QL} + e^{-QL})e^{-z/\ell^*}]. \quad (58)$$

Results for the current density, computed using the MRRF and the DA, are compared in figure 6 and figure 7. In these figures, the current at various points inside and on the surface of the slab is represented by vectors whose length is proportional to the magnitude of the current. The incident beam enters the slab through the face $z = 0$ which crosses at the origin $(z, \rho) = (0, 0)$, as is shown by horizontal black arrows. In figure 6, the widths of the slab are taken to be sufficiently large so that the current at the exit surface is practically indistinguishable for both methods (the results for $L = 50\ell^*$ are not shown because a very good agreement is already obtained for $L = 10\ell^*$). However, inside the slab, the discrepancy in both direction and magnitude of the current can still be quite large i.e. a few ℓ^* from the source. Note that on the plane of incidence (and sufficiently close to the source position), the discrepancy is also large. This behavior is independent of the slab width and is expected to
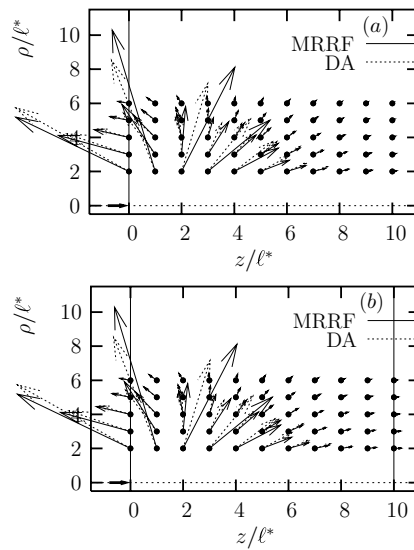
Figure 6. Current $\mathbf{J} = (J_z, J_\rho)$ computed by the MRRF and from the DA for $L = 50\ell^*$ (*a*) and $L = 10\ell^*$ (*b*).

remain even in the case of a half-space. In figure 7, results for thinner slabs are shown. At $L = 5\ell^*$, the discrepancy in both magnitude and direction of the current is clearly visible at the exit surface of the slab.

In figure 8, we plot the normal component of the current J_z at the exit face of the slab ($z = L$) as a function of the transverse separation between the source and the detector, ρ. Both the MRRF and the DA are used. It can be seen that J_z decays exponentially with ρ in both approaches with approximately the same exponent. But when the source and the detector are nearly on axis ($\rho \lesssim \ell^*$), the results notably differ. We note that a similar discrepancy between the experimentally measured transmitted intensity and predictions of the DA has been observed experimentally [33]. This discrepancy is a maximum for on-axis measurements and could not be removed by adjusting the diffusion theory parameters.

6.5. Density

In figure 9, we compare the density of electromagnetic radiation u computed by the MRRF and by Monte Carlo simulations for a slab with $L = 10\ell^*$. The Monte Carlo simulations were performed with the use of the publicly available code MCML [31, 32]. In the figure, we plot u as a function of depth z for different transverse source–detector separations. Reasonable agreement between the two methods is obtained. The small discrepancy can be attributed to imprecisions which are inherent in both methods of solving the RTE.

7. Summary

In this paper, we have shown that the method of rotated reference frames (MRRF) can be used to solve the radiative transport equation in the slab geometry. Numerical results were obtained and validated by comparison with the diffusion approximation and by Monte Carlo simulations. The MRRF was used to compute the specific intensity, as well as the current and
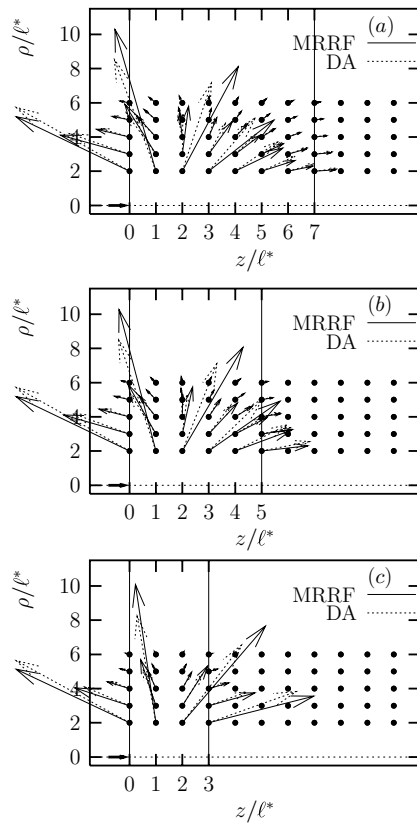
Figure 7. Same as figure 6, but for $L = 7\ell^*$ (*a*), $L = 5\ell^*$ (*b*) and $L = 3\ell^*$ (c).
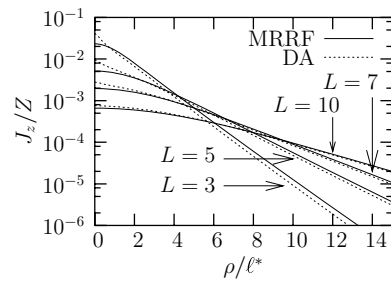

Figure 8. Current component J_z computed at the exit face of the slab ($z = L$) as a function of the transverse source–detector separation ρ, for different values of L, as indicated. Solid lines—MRRF, dotted lines—DA. Normalization factor: $Z = I_0/(\ell^*)^2$.

density of electromagnetic radiation for a narrow collimated beam of light normally incident on the slab. Note that here the specific intensity coincides (up to a multiplicative constant) with the RTE Green's function.

The development of the MRRF and the plane-wave decompositions which were utilized in this paper was motivated by the problem of optical imaging in highly scattering media.
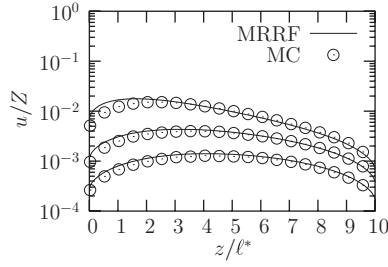
Figure 9. Density $u(z, \rho)$ computed by the MRRF and by Monte Carlo simulations for a slab with $L = 10\ell^*$. From top to bottom, the curves correspond to $\rho = 4\ell^*$, $\rho = 7\ell^*$ and $\rho = 10\ell^*$. Normalization factor: $Z = I_0/(\ell^*)^2$.

The solutions we obtain here are utilized in the formulation of the linearized inverse transport problem [19].

We have computed the current of electromagnetic energy by using the MRRF and the diffusion approximation (DA) for slabs of varying width. When the current is evaluated on the exit surface of the slab (this situation is typical when the transmitted intensity is measured), agreement between the two methods is good, as long as the slab width is sufficiently large, e.g. $L \gtrsim 5\ell^*$, where ℓ^* is the transport mean free path. However, within the slab, the results of MRRF and DA can differ even in very thick slabs; the largest difference is obtained close to the source. However, we have used only the standard DA which is explained, for example, in [6, 29, 30]. It would also be of interest to compare our method with more sophisticated approaches to the DA such as the delta-Eddington approximation [34, 35].

Acknowledgments

Appendix A. Wigner functions and Jacobi polynomials

The mathematical properties and various definitions of the Wigner d-functions are given in [20]. Here we provide the analytic continuation of the Wigner d-functions expressed in terms of Jacobi polynomials to complex angles.

First,

$$
d^l_{mM}(\theta) = [\Theta(M - m) + (-1)^{m+M}\Theta(m - M)]
$$
$$
\times \sqrt{\frac{s!(s + \nu_- + \nu_+)!}{(s + \nu_-)!(s + \nu_+)!}} \left(\frac{1 - \cos\theta}{2}\right)^{\nu_-/2} \left(\frac{1 + \cos\theta}{2}\right)^{\nu_+/2} P_s^{(\nu_-, \nu_+)}(\cos\theta), \quad \text{(A.1)}
$$

where $\Theta(\cdot)$ is the step function, $\nu_- = |m - M|$, $\nu_+ = |m + M|$, and $s = l - (\nu_- + \nu_+)/2$ and $P_s^{(p,q)}(x)$ are the Jacobi polynomials. By analytic continuation, $\cos\theta$ is replaced by $\cos[i\tau(x)]$. Consider the factor $\sqrt{1 \pm \cos[i\tau(x)]}$. We have

$$
\sqrt{1 + \cos[i\tau(x)]} = (\sqrt{1 + x^2} + 1)^{1/2}, \quad \text{(A.2)}
$$

$$
\sqrt{1 - \cos[i\tau(x)]} = i\sqrt{\cos[i\tau(x)] - 1} = i(\sqrt{1 + x^2} - 1)^{1/2} \quad \text{(A.3)}
$$

and, finally,

$$d^l_{mM}[\mathrm{i}\tau(x)] = \mathrm{i}^{\nu_-}[\Theta(M-m) + (-1)^{m+M}\Theta(m-M)]\sqrt{\frac{s!(s+\nu_-+\nu_+)!}{(s+\nu_-)!(s+\nu_+)!}}$$

$$\times \left(\frac{\sqrt{1+x^2}-1}{2}\right)^{\nu_-/2}\left(\frac{\sqrt{1+x^2}+1}{2}\right)^{\nu_+/2}$$

$$\times \sum_{j=0}^{s}\frac{(s+\nu_-)!}{(s-j)!(\nu_-+j)!}\frac{(s+\nu_+)!}{j!(s+\nu_+-j)!}\left(\frac{\sqrt{1+x^2}-1}{2}\right)^{j}\left(\frac{\sqrt{1+x^2}+1}{2}\right)^{s-j}. \tag{A.4}$$

Appendix B. Wigner d-matrix pyramid

To compute the Wigner d-functions for arbitrary indices, we start with $d^0_{00}[\mathrm{i}\tau(x)](=1)$, $d^1_{00}[\mathrm{i}\tau(x)]$, $d^1_{1-1}[\mathrm{i}\tau(x)]$, $d^1_{10}[\mathrm{i}\tau(x)]$ and $d^1_{11}[\mathrm{i}\tau(x)]$. These can be explicitly written as

$$d^1_{00} = \sqrt{1+x^2}, \quad d^1_{1-1} = \frac{1-\sqrt{1+x^2}}{2}, \quad d^1_{10} = -\mathrm{i}\frac{x}{\sqrt{2}}, \quad d^1_{11} = \frac{1+\sqrt{1+x^2}}{2}. \tag{B.1}$$

Next we increase l iteratively up to $l_{\max}$. For each value of l, we first compute $d^l_{mM}[\mathrm{i}\tau(x)]$ ($m = 0, \ldots, l-2$; $M = -m, \ldots, m$) according to

$$d^l_{mM} = \frac{l(2l-1)}{\sqrt{(l^2-m^2)(l^2-M^2)}}$$

$$\times \left[\left(d^1_{00} - \frac{mM}{l(l-1)}\right)d^{l-1}_{mM} - \frac{\sqrt{[(l-1)^2-m^2][(l-1)^2-M^2]}}{(l-1)(2l-1)}d^{l-2}_{mM}\right]. \tag{B.2}$$

Then we obtain $d^l_{ll}[\mathrm{i}\tau(x)]$ and $d^l_{l-1,l-1}[\mathrm{i}\tau(x)]$ as

$$d^l_{ll} = d^1_{11}d^{l-1}_{l-1,l-1}, \qquad d^l_{l-1,l-1} = \left(ld^1_{00} - l + 1\right)d^{l-1}_{l-1,l-1}, \tag{B.3}$$

and $d^l_{lM}[\mathrm{i}\tau(x)](M = l-1, \ldots, -l)$ as

$$d^l_{lM} = -\mathrm{i}\sqrt{\frac{l+M+1}{l-M}}\sqrt{\left|\frac{d^1_{1-1}}{d^1_{11}}\right|}d^l_{l,M+1}. \tag{B.4}$$

Finally, we obtain $d^l_{l-1,M}[\mathrm{i}\tau(x)]$ ($M = l-2, \ldots, 1-l$) from

$$d^l_{l-1,M} = -\mathrm{i}\frac{ld^1_{00}-M}{ld^1_{00}-M-1}\sqrt{\frac{l+M+1}{l-M}}\sqrt{\left|\frac{d^1_{1-1}}{d^1_{11}}\right|}d^l_{l-1,M+1}. \tag{B.5}$$

The remaining functions $d^l_{mM}[\mathrm{i}\tau(x)]$ are obtained by using the symmetry properties

$$d^l_{mM} = d^l_{-M,-m} = (-1)^{m+M}d^l_{-m,-M} = (-1)^{m+M}d^l_{Mm}. \tag{B.6}$$

References

[1] Arridge S R 1999 *Inverse Problems* **15** R41
[2] Sobolev V V 1976 *Light Scattering in Planetary Atmospheres* (International Series of Monographs in Natural Philosophy) (Oxford: Pergamon)
[3] Apresyan L A and Kravtsov Y A 1996 *Radiation Transfer: Statistical and Wave Aspects* (Amsterdam: Gordon and Breach)

 [4] Chandrasekhar S 1960 *Radiative Transfer* (New York: Dover)
 [5] Case K M and Zweifel P F 1967 *Linear Transport Theory* (Massachusetts: Addison-Wesley)
 [6] Ishimaru A 1978 *Wave Propagation and Scattering in Random Media* (San Diego: Academic)
 [7] Williams M M R 2009 *Ann. Nucl. Energy* **36** 767–83
 [8] Ganapol B D and Kornreich D E 2009 *Ann. Nucl. Energy* **36** 1242–55
 [9] Williams M M R 1982 *J. Phys. A: Math. Gen.* **15** 965
[10] Siewert C E and Dunn W L 1983 *Z. A. Math. Phys.* **34** 627–41
[11] Siewert C E and Dunn W L 1989 *J. Quantum Spec. Rad. Trans.* **41** 467–81
[12] Thomas G E and Stanmes K 1999 *Radiative Transfer in the Atmosphere and Ocean* (New York: Cambridge University Press)
[13] Spanier J and Gelbard E M 1969 *Monte Carlo Principles and Neutron Transport Problems* (Massachusetts: Addison-Wesley)
[14] Markel V A 2004 *Waves Random Media* **14** L13–19
[15] Panasyuk G, Schotland J C and Markel V A 2006 *J. Phys. A: Math. Gen.* **39** 115–37
[16] Kim A D and Keller J B 2003 *J. Opt. Soc. Am.* A **20** 92–8
[17] Kim A D 2004 *J. Opt. Soc. Am.* A **21** 820–7
[18] Markel V A and Schotland J C 2004 *Phys. Rev.* E **70** 056616
[19] Schotland J C and Markel V A 2007 *Inverse Problems Imaging* **1** 181–8
[20] Varshalovich D A, Moskalev A N and Khersonskii V K 1988 *Quantum Theory of Angular Momentum* (Singapore: World Scientific)
[21] Ben Israel A and Greville T N E 2003 *Generalized Inverses: Theory and Applications* 2nd ed (New York: Springer)
[22] Penrose R 1955 *Proc. Cambridge Phil. Soc.* **51** 406–13
[23] Moore E H 1920 *Bull. Am. Math. Soc.* **26** 394–5
[24] Leonard I E 1988 *Am. Math. Mon.* **95** 431–3
[25] Henyey L G and Greenstein J L 1941 *Astrophys. J.* **93** 70–83
[26] Courant R and Hilbert D 1953 *Methods of Mathematical Physics* vol 1 (New York: Interscience)
[27] Edmonds A R 1957 *Angular Momentum in Quantum Mechanics* (New York: Princeton University Press)
[28] Blanco M A, Flórez M and Bermejo M 1997 *J. Mol. Struct.* **419** 19
[29] Van Rossum M C W and Nieuwenhuizen T M 1999 *Rev. Mod. Phys.* **71** 313
[30] Markel V A and Schotland J C 2002 *J. Opt. Soc. Am.* A **19** 558
[31] Wang L-H, Jacques S L and Zheng L-Q 1995 *Comput. Methods Programs Biomed.* **47** 131–46
[32] Wang L-H, Jacques S L and Zheng L-Q 1997 *Comput. Methods Programs Biomed.* **54** 141–50
[33] Markel V A, Wang Z and Schotland J C 2005 *Proc. SPIE* **5969** 59691B-1–11
[34] Joseph J H, Wiscombe W J and Weinman J A 1976 *J. Atmos. Sci.* **33** 2452–9
[35] Davis A B 2008 *J. Geophys. Res.* **113** D14S10-1–16